batteries

MDPI

Article

Ag-Doping Effect on MnO_2 Cathodes for Flexible Quasi-Solid-State Zinc-Ion Batteries

Yanxin Liao [1,†], Chun Yang [1,†], Qimeng Xu [1], Wenxuan Zhao [1], Jingwen Zhao [2,3], Kuikui Wang [1,*] and Hai-Chao Chen [1,*]

1 Institute of Materials for Energy and Environment, School of Materials Science and Engineering, Qingdao University, Qingdao 266071, China
2 Qingdao Industrial Energy Storage Research Institute, Qingdao Institute of Bioenergy and Bioprocess Technology, Chinese Academy of Sciences, Qingdao 266101, China
3 Shandong Energy Institute, Qingdao 266101, China
* Correspondence: kkwang@qdu.edu.cn (K.W.); chenhc@qdu.edu.cn (H.-C.C.)
† These authors contributed equally to this work.

Abstract: Rechargeable aqueous Zn/MnO_2 batteries are very potential for large-scale energy storage applications owing to their low cost, inherent safety, and high theoretical capacity. However, the MnO_2 cathode delivers unsatisfactory cycling performance owing to its low intrinsic electronic conductivity and dissolution issue. Herein, we design and synthesize a Ag-doped sea-urchin-like MnO_2 material for rechargeable zinc-ion batteries (ZIBs). Doping Ag was found to reduce charge transfer resistance, increase the redox activity, and improve the cycling stability of MnO_2. The unique sea-urchin-like structure maintains rich active sites for charge storage. As a result, the Ag-doped MnO_2-based ZIB presents a high reversible specific capacity to 315 mA h g^{-1} at 50 mA g^{-1}, excellent rate performance, and a capacity retention of 94.4% when cycling over 500 cycles. An ex situ TEM test demonstrates the low-dissolution property of Ag-doped MnO_2. A flexible quasi-solid-state ZIB is successfully assembled using Ag-doped MnO_2 on graphite paper, which shows a stable specific capacity of 171 mA h g^{-1} at 1 A g^{-1} when cycled over 600 cycles. Our investigation demonstrates the significant role played by Ag doping in enhancing the ZIB performance of MnO_2, and gives some insight into developing advanced active materials by heteroatom doping.

Keywords: zinc-ion batteries; MnO_2; Ag doping; cathode materials

check for updates

Citation: Liao, Y.; Yang, C.; Xu, Q.; Zhao, W.; Zhao, J.; Wang, K.; Chen, H.-C. Ag-Doping Effect on MnO_2 Cathodes for Flexible Quasi-Solid-State Zinc-Ion Batteries. *Batteries* **2022**, *8*, 267. https:///doi.org10.3390/batteries8120267

Academic Editor: Torsten Brezesinski

Received: 29 September 2022
Accepted: 25 November 2022
Published: 2 December 2022

1. Introduction

Growing concerns on environmental issues and increasing demands for renewable energy trigger more research attentions on advanced electrical energy storage systems [1,2]. Rechargeable aqueous zinc-ion batteries (ZIBs) have been actively pursued recently by virtue of their high theoretical capacity, good safety, low cost of raw materials, and low redox potential intrinsic to the zinc metal anode [3,4]. So far, a few kinds of materials have been studied as the cathode materials for ZIBs, such as manganese-based oxides, vanadium-based materials, Prussian blue analogues, and some active organic compounds [5–8]. Among them, manganese-based oxides, especially MnO_2, are perhaps the most attractive candidate for practical applications, considering their combined merits in terms of low cost, environmental benignity, high operation voltage (~1.4 V vs. Zn/Zn^{2+}), and high theoretical capacity (~308 mA h g^{-1}) [9–11]. Liu et al. [12] reported α-MnO_2 as the cathode for ZIBs, exhibiting an operating voltage of 1.44 V along with a maximal capacity to 285 mA h g^{-1}. Chen et al. [13] reported that β-MnO_2 also possesses a high reversible capacity of 225 mA h g^{-1}, while 94% of capacity retention could be achieved when cycled over 2000 cycles.

However, in theory, all MnO_2 polymorphs experience a Jahn–Teller distortion under discharged state, leading to Mn dissolution into the electrolyte followed by rapid capacity

fading [14]. Meanwhile, the MnO_2 cathode suffers from low intrinsic electronic conductivity and strong electrostatic repulsion with Zn^{2+}, resulting in limited Zn ion-storage performance [15]. Previous research efforts have actually sought diverse strategies to premeditatively overcome the instability issues of MnO_2, such as pre-addition of Mn^{2+} into electrolyte [12], surface coating [16,17], defect engineering, and heteroatom doping [18–21]. Heteroatom doping is an effective method to modify the intrinsic physicochemical properties of MnO_2 [22]. Kim et al. reported V-doped MnO_2 via a simple ambient redox reaction [23]. Doping with V atoms not only increased the specific surface area of MnO_2, but also improved its electronic conductivity. Pan et al. found that Ni dopants enabled a higher degree of tetragonal orthorhombic distortion for improved Grotthuss proton transport in the tunnels of α-MnO_2, and the Ni-doped α-MnO_2 delivered a capacity of 303 mA h g^{-1} and impressive specific energy density of 421 W h kg^{-1} [24]. Recently, N and F doping of MnO_2 was pursued, which created additional oxygen vacancies; as a result, improved ion insertion and transport kinetics, as well as enhanced electrical conductivity could be achieved [25,26]. In despite of the fact that heteroatom doping could effectively overcome the intrinsic shortcomings of MnO_2, the performance improvement has been restricted by the limited choice of the heteroatom types that can be well distributed in the MnO_2 bulk phase. Thus, it is desirable to develop new and efficient dopants for better performance of MnO_2. Ag has an excellent conduction nature, and doping Ag has been proved to enhance the electronic conductivity, increase the formation of more oxygen vacancies, and modify the band gap of electrode materials, which has been successfully applied in supercapacitors [27], catalysts [28], solar cells [29]. In addition, the morphologies and particle sizes of MnO_2 also have effects on electrochemical performance of ZIBs [22]. It is reported that iron-doped hollow sea-urchin-like MnO_2 with many nanowires extended from a common center process larger surface area which can provide more active sites for electrochemical reaction, showing good electrochemical performance for supercapacitors [30].

Here, Ag-doped MnO_2 with a sea-urchin-like structure was synthesized via a simple hydrothermal method, which was first utilized as a cathode material for ZIBs. A series of characterizations indicate that not only a unique sea-urchin-like structure provides more active sites, but also doping Ag heteroatoms improves the ionic conductivity of MnO_2. Besides, the Ag redox in charge/discharge has contributed to increased capacity., leading to improved electrochemical Zn^{2+} insertion and transport kinetics. As a result, by tuning the Ag-doping content, the Ag-doped MnO_2-based ZIB delivers high reversible specific capacity (315 mA h g^{-1} at 50 mA g^{-1}), enhanced cyclic stability (500 cycles with the capacity retention of 94.4%), and excellent rate performance. In addition, flexible quasi-solid-state ZIBs are successfully assembled based on graphite papers supported by Ag-doped MnO_2, which exhibits a stable capacity of 171 mA h g^{-1} at 1 A g^{-1} over 600 cycles.

2. Experimental

2.1. Synthesis of Ag-Doped Sea-Urchin-like MnO_2 and Pure MnO_2

First, $MnSO_4$ (0.48 g, AR), $(NH_4)_2S_2O_8$ (0.73 g, AR) and 80 mL of deionized water were put into a beaker and stirred to make the reactant totally dissolved. Then, 3.2 mL of concentrated H_2SO_4 (98%) was slowly added into the beaker. Then, 1, 3, 5, 7, 9 wt.% of $AgNO_3$ (AR) was dissolved into 1.6 mL of deionized water and added into above solution. The solution was put into a Teflon contained autoclave and heated at 120 °C for 6 h. The precipitates were collected, washed with deionized water and absolute ethanol, respectively, several times to remove impurities, and then dried at 60 °C overnight. Pure MnO_2 was synthesized following a same procedure without adding $AgNO_3$. The products designated as 1%Ag-MnO_2, 3%Ag-MnO_2, 5%Ag-MnO_2, 7%Ag-MnO_2, 9%Ag-MnO_2 and MnO_2, respectively. In addition, 5%Ag-MnO_2 samples were also synthesized using different reaction time of 1, 2, and 4 h.

2.2. Synthesis of the Polyacrylamide (PAM) Hydrogel Electrolyte

Typically, acrylamide (15 g, 99%), N,N′-methylenebisacrylamide (10 mg, AR) and potassium persulfate (75 mg, AR) were dissolved in 50 mL of deionized water and stirred to make the reactant totally dissolved. PAM was obtained after polymerization at 60 °C for 60 min.

2.3. Synthesis of the Flexible Zn Anode

The flexible Zn anode was prepared by an electrodeposition method [31]. $ZnSO_4 \cdot 7H_2O$ (10.23 g, AR) and $Na_3C_6H_5O_7 \cdot 2H_2O$ (14.7 g, AR) were put into 100 mL of deionized water with magnetic stirring. Chronoamperometry was applied to electrodeposit Zn on carbon cloth substrates at −1.4 V (vs. saturated calomel electrode) for 15 min.

2.4. Materials Characterizations

The crystal structures of the electrodes were characterized by the X-ray diffraction (XRD; Rigaku, Ultima IV, Tokyo, Japan; Cu Kα radiation λ = 0.15418 nm) technique. The morphology of samples was investigated by field-emission scanning electron microscope (FESEM; JEOL, JSM-7800F, Tokyo, Japan) and transmission electron microscope (TEM; JEOL, JEM-2100 plus). The element compositions of samples were tested by X-ray photoelectron spectroscopy (XPS; PHI5000 Versaprobe III). The Raman spectra were tested using a Raman spectroscopy (Renishaw inVia Raman spectrometer) at a laser wavelength of 532 nm.

2.5. Electrochemical Measurements

The cathodes were prepared by mixing active materials, acetylene black and polyvinylidene fluoride (PVDF) at an appropriate weight ratio of 7:2:1. The mixture was uniformly coated on titanium mesh and dried, at 80 °C, overnight. The mass loading of active material per electrode was about 2 mg cm^{-2}. The electrochemical properties were measured in 2032-type coin cells using Zn metal plate as anode, glass fiber as separator and 2 M $ZnSO_4$ with 0.1 M $MnSO_4$ additive as electrolyte. The discharge and charge performance was measured on a multi-channel battery test system (Neware CT-4008 W, Shenzhen, China) in the voltage range of 0.8–1.8 V vs. Zn/Zn^{2+}. Cyclic voltammetry (CV) and Electrochemical Impedance Spectroscopy (EIS) measurements were taken on CHI660E. All these tests were carried out at room temperature.

3. Results and Discussion

The Ag-doped MnO_2 and pure MnO_2 were synthesized by a simple hydrothermal method, and the synthesis route was illustrated in Figure 1a. The XRD patterns of Ag-doped MnO_2 and pure MnO_2 are shown in Figure S1, the MnO_2 exhibits apparent diffraction peaks at 12.4°, 17.8°, 28.4°, 36.3°,37.3°, 41.6°,49.4°, 55.1°, 59.8°, 65.1°, 69.0°, and 72.6°, which can be assigned to the (110), (200), (310), (400), (211), (301), (411), (600), (521), (002), (541), and (312) planes of α-MnO_2 (space group: Tetragonal I4/m, JCPDS: 44–0141). The Ag-doped MnO_2 samples exhibit same XRD patterns compared with pure MnO_2 without any additional peaks, indicating the crystal structure of MnO_2 can be maintained when doped with Ag. However, the diffraction peaks from (110), (200), (400), (301), (600) planes weakens and become much broader when increased Ag dopant was used, indicating decreased grain size and increased amount of lattice defects [32]. The diffraction peak located at 37.3° intensifies after doping with Ag, indicating preferred orientation growth of (211) plane. Moreover, the diffraction peaks from (411), (600), and (521) planes gradually shift to a high diffraction angle when doped with increased amounts of Ag, indicating increased lattice distortion of MnO_2 unit cell [33,34]. To identify lattice distortion degree and location of the Ag dopant in the unit cell, the refinement XRD patterns of pure MnO_2 and 5%Ag-MnO_2 are presented in Figure 1b,c. The refinement crystal structures of pure MnO_2 and 5%Ag-MnO_2 can be found in the inset of Figure 1b,c, respectively. The Rietveld-refined fractional atomic parameters of 5%Ag-MnO_2 are recorded in Table S1. It is found that 10% of Mn sites are substituted by Ag. Refined parameters for pure MnO_2 are calculated to be a = 9.94 Å,

b = 9.94 Å, c = 2.87 Å, α = 90°, β = 90°, and γ = 90°. However, the lattice parameters are transformed to a = 9.91 Å, b = 9.91 Å, c = 2.87 Å, α = 90°, β = 90°, and γ = 90°, when doped with Ag. Raman spectra of Ag-doped MnO_2 and pure MnO_2 are shown in Figure 1d. The peak at 640 cm^{-1} belongs to the stretching vibration of Mn-O, which exhibits an obvious blueshift for MnO_2 doped with increased amounts of Ag owing to increased Mn^{3+} content [35,36]. Chemical composition and their surface electronic states were analyzed by XPS spectra. Photoelectron emission peak from Ag element can be positively observed in the wide-scan spectrum of 5%Ag-MnO_2 (Figure S2), confirming successful doping of Ag into MnO_2. Figure 1e presents the high-resolution XPS spectrum from Ag 3d electrons of 5%Ag-MnO_2. The peaks at 367.6 and 373.6 eV belong to $3d_{5/2}$ and $3d_{3/2}$ photoelectrons of Ag^+, respectively [37]. Meanwhile, the peaks at 368.3 and 374.3 eV correspond to the standard values of metallic Ag [38]. As shown in Figure 1f, the high-resolution Mn 3s spectrum of 5%Ag-MnO_2 exhibits a spin-energy separation of 4.9 eV, which is higher than that of pure MnO_2. Therefore, Mn elements in 5%Ag-MnO_2 has a lower chemical valence than that in pure MnO_2 owing to Ag doping [39]. The high-resolution O 1s spectrum can be fitted into three peaks (Figure 1g). The peaks of 529.6, 531.1, and 532.7 eV are related to Mn-O, oxygen defects, and adsorbed water [40]. The calculated area ratios of oxygen defects increase from 19% to 23% after introducing Ag into MnO_2. Increased amount of oxygen defect will give rise to narrower band gap and faster electron migration rates, and thus higher reaction activity and fast reaction kinetics can be anticipated for 5%Ag-MnO_2 [41].

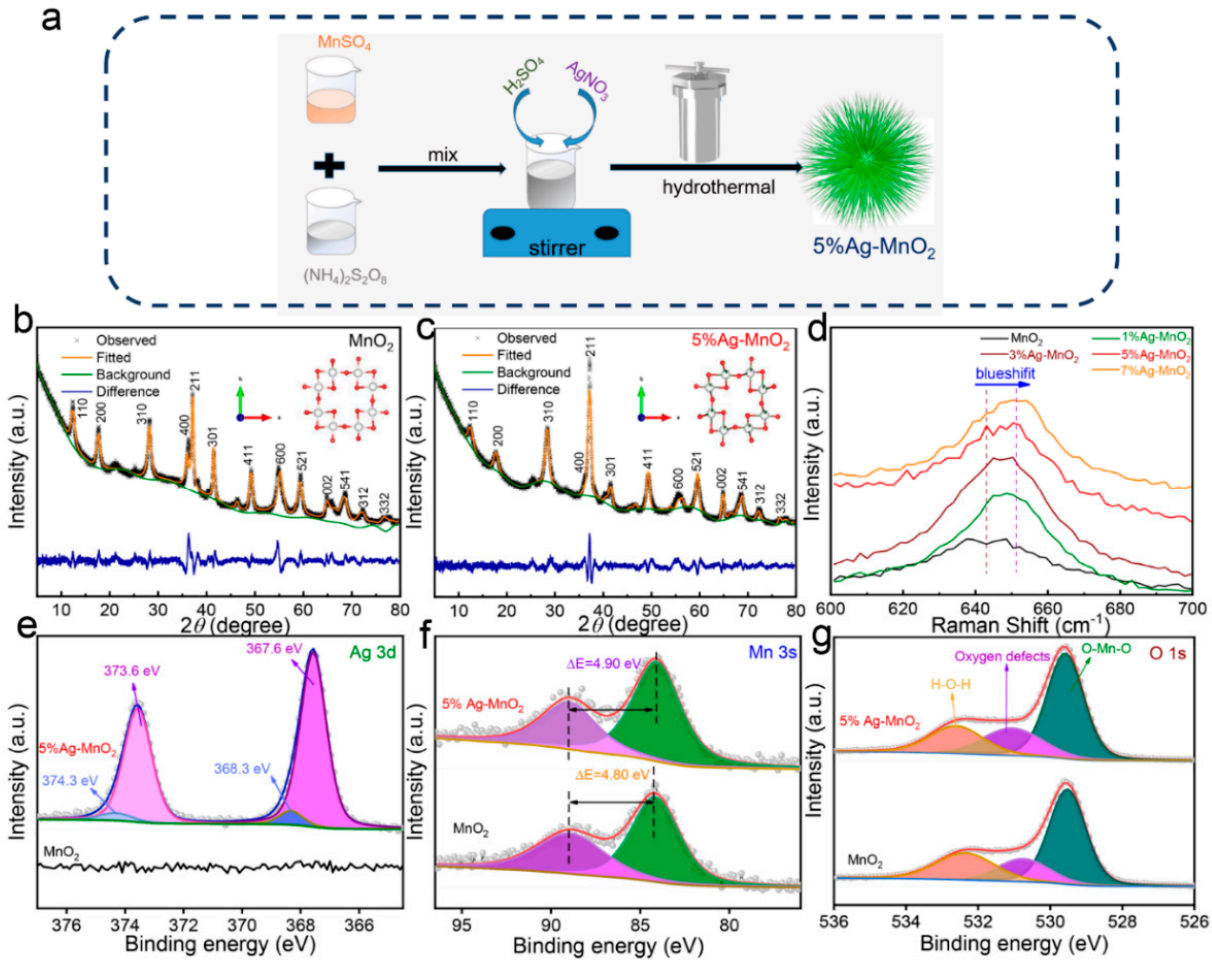

Figure 1. (**a**) Schematic illustration for the synthetic process of 5%Ag-MnO_2. Rietveld refinement results of (**b**) pure MnO_2 and (**c**) 5%Ag-MnO_2, and corresponding crystal structures are presented in the inset. (**d**) Raman spectra of pure MnO_2 and Ag-doped MnO_2. High-resolution (**e**) Ag 3d, (**f**) Mn 3s, and (**g**) O 1s XPS spectra of pure MnO_2 and 5%Ag-MnO_2.

Figure 2a,b show the FESEM images of pure MnO_2. Pure MnO_2 exhibits a sea-urchin-like structure which is composed of many nanowires. The 5%Ag-MnO_2 also displays a sea-urchin-like structure; however, increased amounts of nanowires extended from a common center (Figure 2d,e). It is important to say that the weight ratio of Ag dopant has a great influence on the overall morphology of Ag-doped MnO_2, and only the 5%Ag-MnO_2 sample can form a complete sea-urchin-like structure. Note to say, the morphology does not change with reaction time, we also synthesized the 5%Ag-MnO_2 sample at reaction time of 1, 2, and 4 h, and they exhibit a same sea-urchin-like structure (Figure S3). The reaction time of 6 h is chosen for sample synthesis so as to ensure full precipitation of Mn^{2+}. The sea-urchin-like structure of other Ag-doped MnO_2 all cracked into different segments (Figure S4). Energy-dispersive X-ray spectroscopy (EDS) pattern of 5%Ag-MnO_2 verifies the coexistence of Ag, Mn, and O (Figure S5), and the corresponding EDS mapping images (Figure 2h) display uniform distribution of these elements. TEM images (Figure 2c,f) further verify a sea-urchin-like overall structure of pure MnO_2 and 5%Ag-MnO_2, while more nanowires can be observed on the sea-urchin-like structure for 5%Ag-MnO_2. High-resolution TEM image in Figure 2g shows clear lattice fringes with the space of 0.49 nm, which is corresponding to (200) plane of α-MnO_2. In addition, N_2 adsorption–desorption isotherms (Figure S6) of 5%Ag-MnO_2 and pure MnO_2 samples are both exhibit a type IV isotherm with a H3-type hysteresis loop. The 5%Ag-MnO_2 has a comparable Brunauer–Emmett–Teller (BET) area to pure MnO_2 with a surface area of 58.4 m^2 g^{-1} delivered. However, the 5%Ag-MnO_2 has more mesopores in pore size range of 2–35 nm compared to pure MnO_2. As Zn^{2+} is bivalent with a large radius when the ion is hydrated, relative large pores may promote electrochemical reactions and efficient penetration of the electrolyte into active material [42].

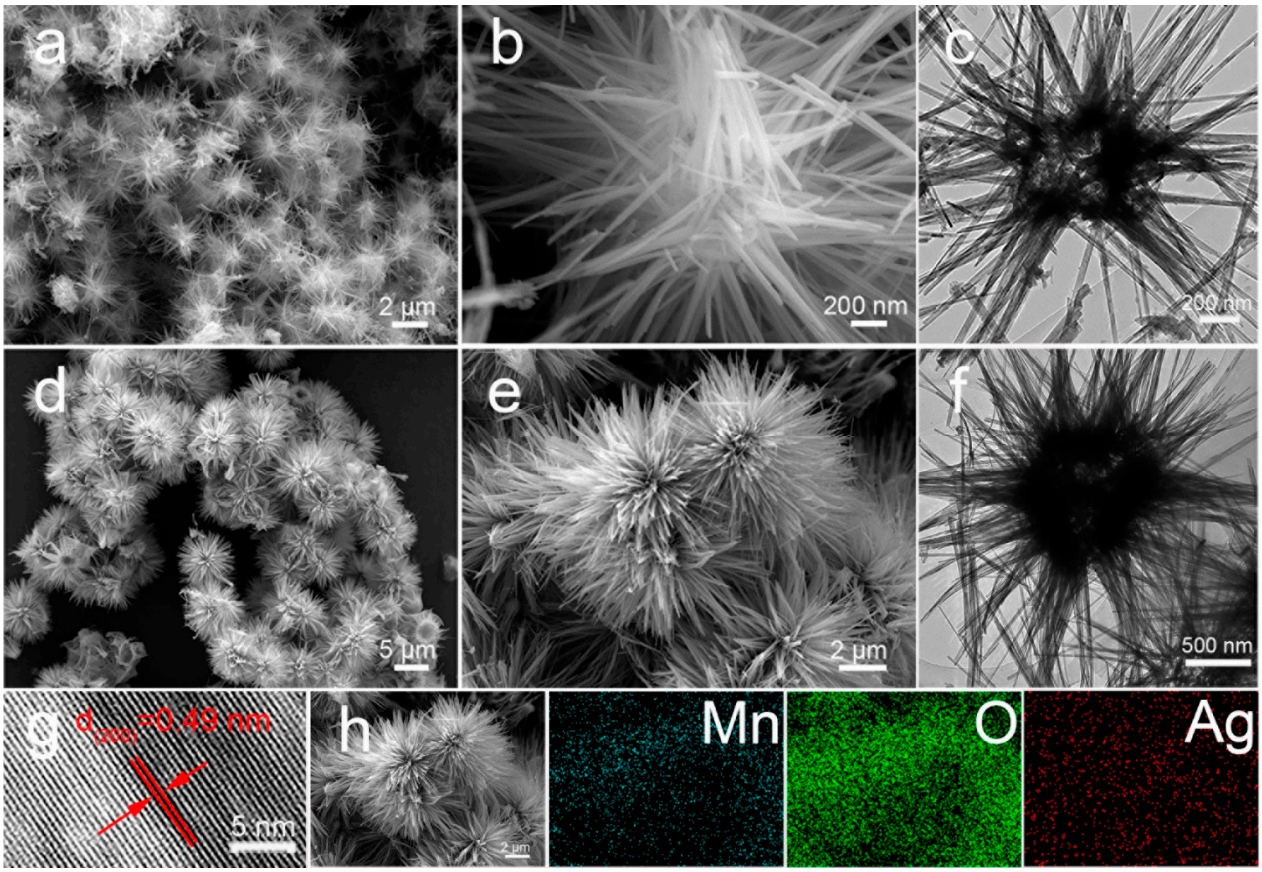

Figure 2. (**a**,**b**) FESEM image of pure MnO_2. (**c**) TEM image of pure MnO_2. (**d**,**e**) FESEM image of 5%Ag-MnO_2. (**f**) TEM image of 5%Ag-MnO_2. (**g**) High-resolution TEM image of 5%Ag-MnO_2. (**h**) EDS elemental mapping images of every element in 5%Ag-MnO_2.

These Ag-doped MnO_2 and pure MnO_2 were used as the zinc-ion host materials in CR2032 coin cells to investigate their energy storage performance in 2 M $ZnSO_4$ electrolyte with 0.1 M $MnSO_4$ additive. Figure 3a shows initial two cycles of CV curves at a scan rate of 0.3 mV s^{-1} for 5%Ag-MnO_2 and pure MnO_2-based ZIBs. The first cycle of CV curve both exhibit two pairs of redox peaks, indicating a two-step electrochemical reaction of above two cathode materials [43]. Compared with pure MnO_2-based ZIB, the Zn/5%Ag-MnO_2-based ZIB exhibits higher potentials for cathodic peaks, while lower potentials for anodic peaks. In addition, there are a couple of weak redox peaks at 0.92 V and 1.16 V exist in the CV curve of 5%Ag-MnO_2-based ZIB, manifesting the successful doping of Ag into MnO_2 (Figure S7). The redox couple of Ag^+/Ag from the Ag dopant provides an additional reaction for energy storage. Meanwhile, the CV curves of 5%Ag-MnO_2-based ZIB shows intensified redox peaks and larger enclosed area than that of ZIB based on pure MnO_2, indicating that reaction activity is enhanced through Ag doping. Figure 3b shows the galvanostatic charge/discharge (GCD) curves of ZIBs based on pure MnO_2 and Zn/5%Ag-MnO_2 at a specific current of 50 mA g^{-1}. The Zn/5%Ag-MnO_2 cell shows a discharge capacity of 315 mA h g^{-1} which is about 22% higher than that of Zn/MnO_2 cell (259 mA h g^{-1}). Furthermore, the polarization value between the discharge and charge plateau is lower after Ag doping owing to improved ion insertion and transport kinetics. Compared to the GCD curves of Zn/MnO_2 cell, the additional discharge plateau at around 0.93 V and charge plateau at around 1.15 V (Figure S8) in the GCD curve of Zn/5%Ag-MnO_2 cell correspond to the reversible redox reaction of Ag dopant. Electrochemical impedance spectroscopy (EIS) measurements (Figure 3c) are used to investigate the charge transfer rate and ion diffusion kinetics, and the charge-transfer resistance (R_{ct}) of 5%Ag-MnO_2 (R_{ct} = 16 Ω) is lower than that of pure MnO_2 (R_{ct} = 26 Ω), indicating improved reaction kinetics for MnO_2 when doped with Ag. The rate performance of ZIBs based on 5%Ag-MnO_2 and pure MnO_2 are shown in Figure 3d. The specific capacity of both two ZIBs increase in initial cycles because of the active progress of cathodes. The 5%Ag-MnO_2-based ZIB delivers specific capacities of 315, 290, 250, 215, 177, 128, and 85 mA h g^{-1} at specific currents of 0.05, 0.1, 0.2, 0.3, 0.5, 1.0, and 2.0 A g^{-1}, respectively; this ZIB shows a specific capacity of 341 mA h g^{-1} when the specific current returns back to 0.05 A g^{-1}. Above capacity values are much higher than the performance achieved by pure MnO_2. Doping Ag increases the redox activity of Mn ions in MnO_2, resulting in a high specific capacity. In addition, inevitably, the deposition of pre-added Mn^{2+} ions may contribute to extra capacity, resulting in a capacity of Ag-doped electrodes higher than the theoretical capacity of MnO_2. Figure 3e shows the long-term cycling performance at 0.5 A g^{-1} for Ag-doped MnO_2 and pure MnO_2. MnO_2 with different Ag-doped amounts all exhibit better cycling performance than the pure MnO_2, especially for the ZIB based on 5%Ag-MnO_2. The 5%Ag-MnO_2-based ZIB presents a specific capacity around 150 mA h g^{-1} over 500 cycles with a capacity retention of 94.4% can be achieved, which is better than most Mn-based and heteroatom doping cathodes (Table S2), while a capacity retention of 76.1% is achieved by pure MnO_2. Better cycling performance of 5%Ag-MnO_2 was further verified by the cycling performance under large specific current of 0.8 A g^{-1} (Figure S9). The morphology of 5%Ag-MnO_2 was also characterized by TEM test when cycling for different cycles. Owing to the Jahn–Teller distortion under discharged state, the original MnO_2 will dissolve into electrolyte when cycling within 50 cycles [14]. However, many nanowires still can be found when the electrode cycled for 50 to 500 cycle, as shown in Figure 3f–i, indicating stable cycling stability of 5%Ag-MnO_2.

To understand the energy storage mechanism of the 5%Ag-MnO_2 electrode, ex situ XRD analysis was conducted during the initial two cycles. As shown in Figure 4a, a set of diffraction peaks appear when discharged to 1.25 V during the first discharge cycle, and their intensity increases continuously until the ZIB is discharged to 0.8 V. In the meantime, the diffraction peaks from α-MnO_2 weakens during the discharge process. The set of newly appeared diffraction peaks can be attributed to $Zn_4SO_4(OH)_6{\cdot}5H_2O$ (PDF#78-0246 and PDF#39-0688), as shown in Figure 4b, which is a typical by-product in ZIBs [44]. The

presence of $Zn_4SO_4(OH)_6{\cdot}5H_2O$ indicates relative alkaline environment near the electrode surface created by insertion of H^+, and this reaction mechanism can be evidenced by the newly formed peak at 21.2° during discharge process, which can be assigned to α-MnOOH (PDF#24-0713). In the first charge process, the diffraction peaks from $Zn_4SO_4(OH)_6{\cdot}5H_2O$ weakens as the voltage increases, and those from α-MnOOH disappears when the voltage charged to 1.6 V. In the voltage region of 0.8–1.8 V, the diffraction peaks from 5%Ag-MnO_2 gradually intensifies as the voltage is increasing. Meanwhile, as shown in Figure 4c, a new peak located at 32.0° is formed at the charge voltage of 1.6 V, which can be attributed to the AgO phase (PDF#76-1489). Therefore, the Ag dopant participates in the redox reaction like a zinc-silver battery [45], and its reaction equation can be written as $2Ag + H_2O–2e^- \leftrightarrow Ag_2O+2H^+$. The signal of Ag cannot be found at full discharge state, which is the possible result of its low content and the strong diffraction peaks of $Zn_4SO_4(OH)_6{\cdot}5H_2O$. In the second cycle, the charge–discharge process is highly reversible. The diffraction peaks of α-MnOOH are observed when the discharge and charge voltages are lower than 1.3 and 1.6 V, respectively. Considering the Zn^{2+} in the electrolyte is prerequisite for energy storage, the discharge/charge plateaus at high voltages are attributed to Zn^{2+} intercalation/extraction, while these at low voltages belong to H^+ intercalation/extraction [15,46].

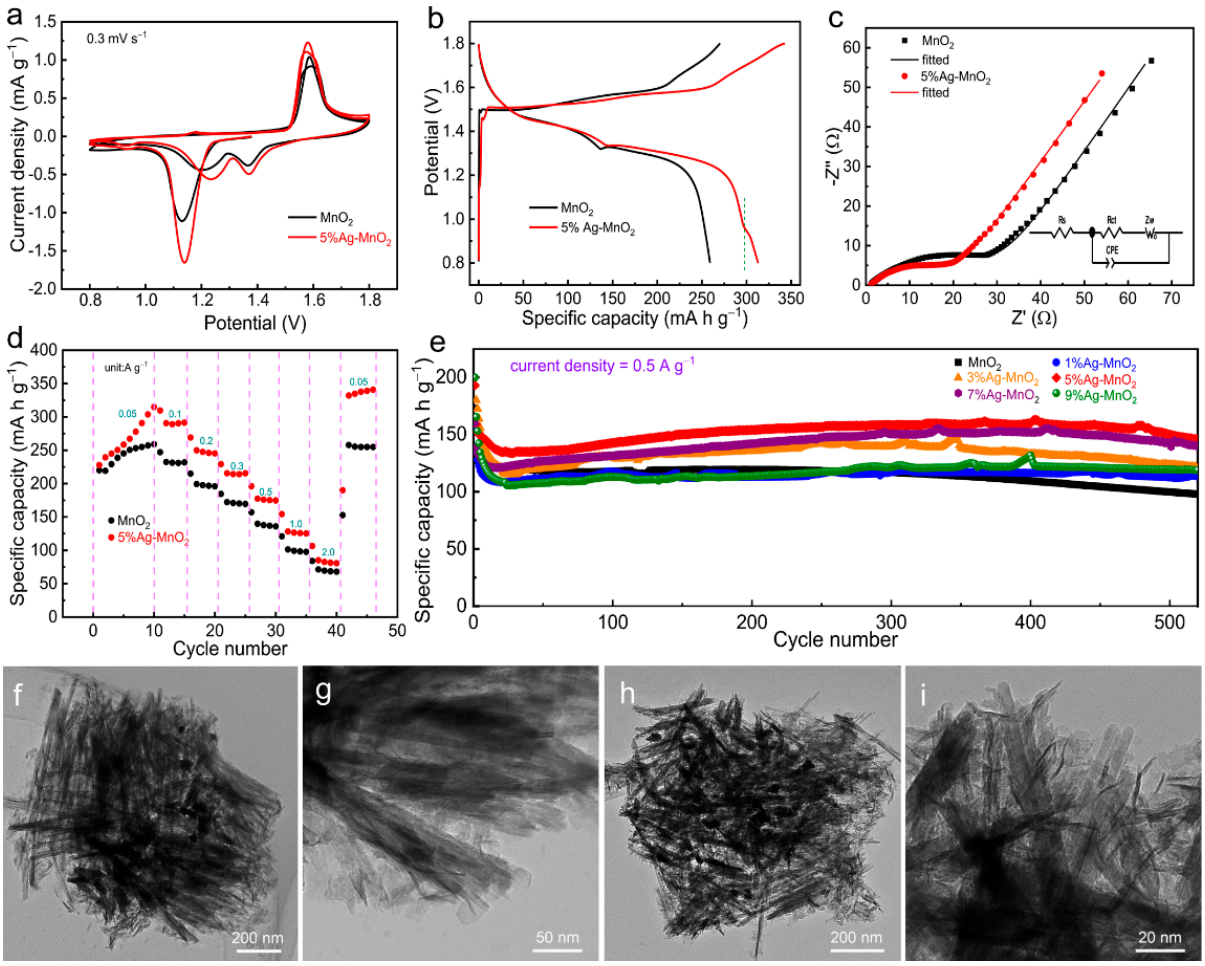

Figure 3. (**a**) CV curves at a scan rate of 0.3 mV s^{-1}, (**b**) GCD curves at a specific current of 0.05 A g^{-1}, (**c**) EIS spectra, and (**d**) rate performances of ZIBs based on pure MnO_2 and 5%Ag-MnO_2. (**e**) Long-term cycling performance at a specific current of 0.5 A g^{-1} for the MnO_2 doped with different amounts of Ag. TEM images of 5%Ag-MnO_2 after being cycled at 0.5 A g^{-1} for (**f**,**g**) 50 and (**h**,**i**) 500 cycles.

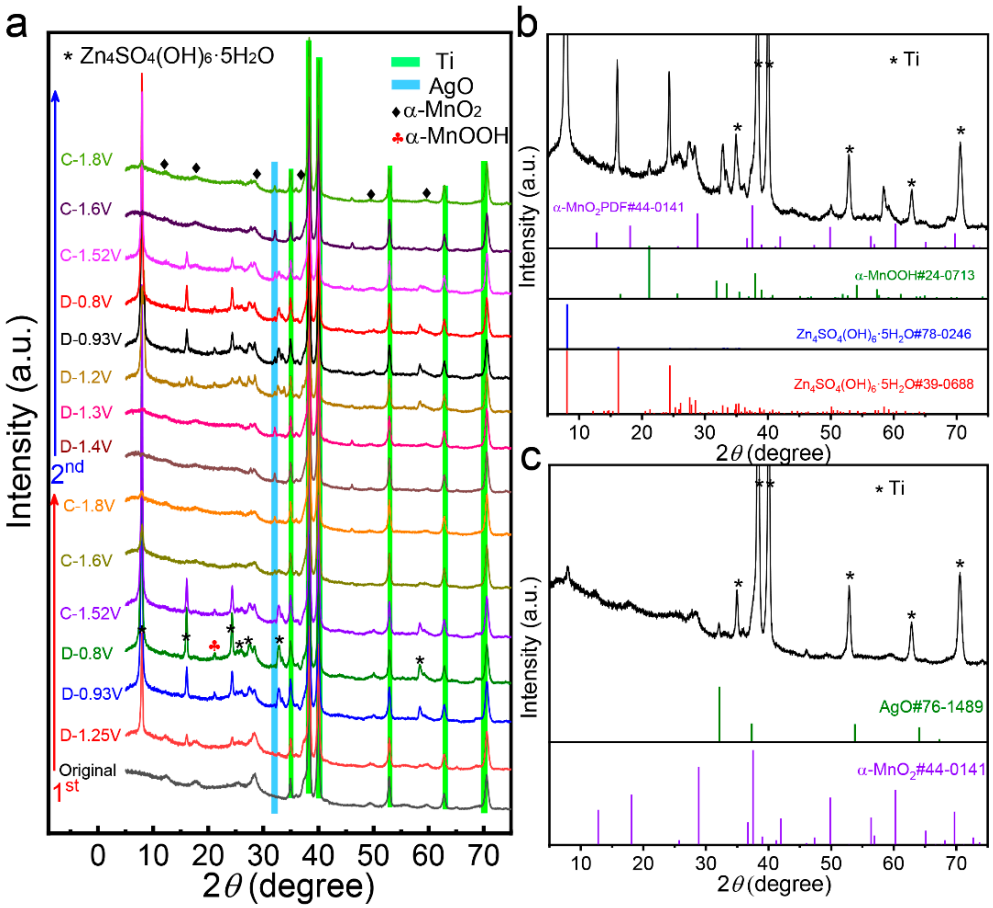

Figure 4. (**a**) Ex situ XRD patterns at different potentials of 5%Ag-MnO_2 during the initial two cycles. XRD pattern of 5%Ag-MnO_2 at full (**b**) discharged and (**c**) charged stage, where the standard XRD pattern is also provided.

In addition, a flexible quasi-solid-state ZIB is successfully assembled using 5%Ag-MnO_2@graphite paper as cathode, Zn@cabon cloth as anode, and polyacrylamide as electrolyte (Figure 5a). As shown in Figure S10, the Zn particles are uniformly deposited on carbon cloth, and the XRD pattern of the electrode can be assigned to pure Zn metal (PDF#87-0713), indicating successful electrodeposition of Zn metal on carbon cloth without any impurities. The quasi-solid-state ZIB shows good flexiblity, which can be blended into different shapes, as shown in Figure 5b. The flexible ZIB has a high open circuit potential to 1.57 V (Figure 5c). As shown in Figure 5d, our quasi-solid-state ZIB can light a red light-emitting diode (LED) indicator under bending. Meanwhile, the flexible quasi-solid-state ZIB exhibits excellent cycling performance with a specific capacity of 171 mA h g^{-1} and nearly 100% of coulombic efficiency maintained at 1 A g^{-1} over 600 cycles (Figure 5e), which is better than most of other flexible quasi-solid-state aqueous ZIBs as shown in Table S3.

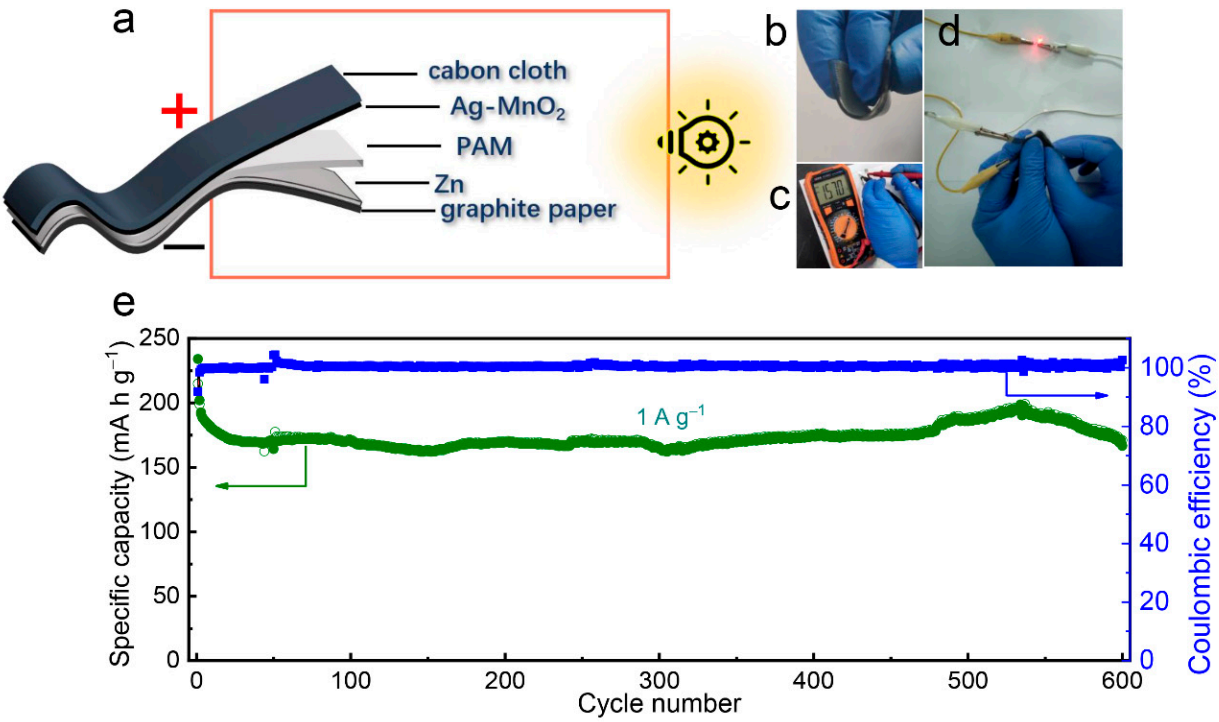

Figure 5. (**a**) Schematic diagram for the structure of our flexible quasi-solid-state ZIB. Photographs of the flexible quasi-solid-state ZIB (**b**) under bending condition, (**c**) showing the open circuit potential, and (**d**) used to drive a red LED under bending condition. (**e**) Long-term cycling performance and coulombic efficiency at 1 A g^{-1} of the flexible quasi-solid-state ZIB.

4. Conclusions

Ag-doped MnO_2 with a sea-urchin-like structure was designed by a hydrothermal method, which shows improved electrochemical behaviours as the cathode material for ZIBs. Upon Ag doping, the electron distribution of MnO_2 was finely tuned, resulting in reduced electrostatic repulsion for Zn^{2+} intercalation and lower charge transfer resistance. As a result, the Zn/5%Ag-MnO_2 ZIB presents highly reversible specific capacity (315 mA h g^{-1} at 50 mA g^{-1}), enhanced cyclic stability (500 cycles with the capacity retention of 94.4%), and excellent rate performance. Moreover, the 5%Ag-MnO_2 is used to assemble flexible quasi-solid-state ZIBs, which exhibit outstanding mechanical flexibility and cyclability with a stable specific capacity of 171 mA h g^{-1} achieved when cycled over 600 cycles.

Supplementary Materials: The following supporting information can be downloaded at: https://www.mdpi.com/article/10.3390/batteries8120267/s1, Figure S1: XRD patterns of pure MnO_2 and Ag-doped MnO_2, and the enlarged view of 411, 521, and 600 diffraction peaks; Figure S2: XPS survey spectrum of pure MnO_2 and 5%Ag-MnO_2; Figure S3 FESEM images of 5%Ag-MnO_2 synthesized at different reaction time of 1, 2, and 4 h; Figure S4: FESEM images of (a) 1%Ag-MnO_2, (b) 3%Ag-MnO_2, (c) 7%Ag-MnO_2, (d) 9%Ag-MnO_2; Figure S5: EDS spectrum of 5%Ag-MnO_2; Figure S6: (a) N_2 adsorption–desorption isotherms and (b) pore size distribution curves of pure MnO_2 and 5%Ag-MnO_2; Figure S7: CV curves at a scan rate of 0.3 mV s^{-1} of ZIBs based on (a) pure MnO_2 and (b) 5%Ag-MnO_2; Figure S8: Galvanostatic charge curves of pure MnO_2 and 5%Ag-MnO_2 around 1.15 V; Figure S9: Long-term cycling performance of pure MnO_2 and 5%Ag-MnO_2 at 0.8 A g^{-1}; Figure S10: XRD pattern and (b) FESEM image of the Zn/carbon cloth electrode; Table S1: Fractional atomic parameters of 5%Ag-MnO_2 with I4/m space group; Table S2: Cycling performance of 5%Ag-MnO_2 compared with reported Mn-based cathodes for ZIBs; Table S3: Cycling performance of our flexible quasi-solid-state ZIB compared with other flexible quasi-solid-state aqueous ZIBs.

Author Contributions: Conceptualization, Y.L. and H.-C.C.; methodology, Y.L., C.Y. and H.-C.C.; validation, Q.X. and W.Z.; investigation, Y.L., H.-C.C. and C.Y.; data curation, Q.X. and W.Z.; writing—original draft preparation, Y.L.; writing—review and editing, H.-C.C., K.W. and J.Z.; supervision, H.-C.C. and K.W.; funding acquisition, H.-C.C., K.W. and J.Z. All authors have read and agreed to the published version of the manuscript.

Funding: This research was funded by National Natural Science Foundation of China, grant number 21905148, 51801108 and 21975271; Shandong Natural Science Foundation, Grant No. ZR2020ZD07. J. W. Zhao particularly acknowledges the financial support from the Youth Innovation Promotion Association of CAS (2019214) and Shandong Energy Institute (Grant No. SEI I202127).

Data Availability Statement: All collected data are presented in the manuscript.

Conflicts of Interest: The authors declare no conflict of interest.

References

1. Larcher, D.; Tarascon, J.M. Towards greener and more sustainable batteries for electrical energy storage. *Nat. Chem.* **2015**, *7*, 19–29. [CrossRef] [PubMed]
2. Chae, M.S.; Hong, S.-T. Prototype System of Rocking-Chair Zn-Ion Battery Adopting Zinc Chevrel Phase Anode and Rhombohedral Zinc Hexacyanoferrate Cathode. *Batteries* **2019**, *5*, 3. [CrossRef]
3. Cao, Z.; Zhuang, P.; Zhang, X.; Ye, M.; Shen, J.; Ajayan, P.M. Strategies for dendrite-free anode in aqueous rechargeable zinc ion batteries. *Adv. Energy Mater.* **2020**, *10*, 2001599. [CrossRef]
4. Tang, B.; Shan, L.; Liang, S.; Zhou, J. Issues and opportunities facing aqueous zinc-ion batteries. *Energy Environ. Sci.* **2019**, *12*, 3288–3304. [CrossRef]
5. Jia, X.; Liu, C.; Neale, Z.G.; Yang, J.; Cao, G. Active Materials for Aqueous Zinc Ion Batteries: Synthesis, Crystal Structure, Morphology, and Electrochemistry. *Chem. Rev.* **2020**, *120*, 7795–7866. [CrossRef] [PubMed]
6. Konarov, A.; Voronina, N.; Jo, J.H.; Bakenov, Z.; Sun, Y.-K.; Myung, S.-T. Present and Future Perspective on Electrode Materials for Rechargeable Zinc-Ion Batteries. *ACS Energy Lett.* **2018**, *3*, 2620–2640. [CrossRef]
7. Liu, B. Transition Metal Dichalcogenides for High−Performance Aqueous Zinc Ion Batteries. *Batteries* **2022**, *8*, 62. [CrossRef]
8. Parveen, N.; Ansari, S.A.; Ansari, M.Z.; Ansari, M.O. Manganese oxide as an effective electrode material for energy storage: A review. *Environ. Chem. Lett.* **2022**, *20*, 283–309. [CrossRef]
9. Kang, L.; Cui, M.; Zhang, Z.; Jiang, F. Rechargeable Aqueous Zinc-Ion Batteries with Mild Electrolytes: A Comprehensive Review. *Batter. Supercaps* **2020**, *3*, 966–1005. [CrossRef]
10. Zeng, X.; Hao, J.; Wang, Z.; Mao, J.; Guo, Z. Recent progress and perspectives on aqueous Zn-based rechargeable batteries with mild aqueous electrolytes. *Energy Storage Mater.* **2019**, *20*, 410–437. [CrossRef]
11. Fitz, O.; Ingenhoven, S.; Bischoff, C.; Gentischer, H.; Birke, K.P.; Saracsan, D.; Biro, D. Comparison of Aqueous- and Non-Aqueous-Based Binder Polymers and the Mixing Ratios for Zn//MnO_2 Batteries with Mildly Acidic Aqueous Electrolytes. *Batteries* **2021**, *7*, 40. [CrossRef]
12. Pan, H.; Shao, Y.; Yan, P.; Cheng, Y.; Han, K.S.; Nie, Z.; Wang, C.; Yang, J.; Li, X.; Bhattacharya, P.; et al. Reversible aqueous zinc/manganese oxide energy storage from conversion reactions. *Nat. Energy* **2016**, *1*, 16039. [CrossRef]
13. Zhang, N.; Cheng, F.; Liu, J.; Wang, L.; Long, X.; Liu, X.; Li, F.; Chen, J. Rechargeable aqueous zinc-manganese dioxide batteries with high energy and power densities. *Nat. Commun.* **2017**, *8*, 405. [CrossRef]
14. Liao, Y.; Chen, H.-C.; Yang, C.; Liu, R.; Peng, Z.; Cao, H.; Wang, K. Unveiling performance evolution mechanisms of MnO_2 polymorphs for durable aqueous zinc-ion batteries. *Energy Storage Mater.* **2022**, *44*, 508–516. [CrossRef]
15. Fang, G.; Zhou, J.; Pan, A.; Liang, S. Recent Advances in Aqueous Zinc-Ion Batteries. *ACS Energy Lett.* **2018**, *3*, 2480–2501. [CrossRef]
16. Wu, B.; Zhang, G.; Yan, M.; Xiong, T.; He, P.; He, L.; Xu, X.; Mai, L. Graphene Scroll-Coated α-MnO_2 Nanowires as High-Performance Cathode Materials for Aqueous Zn-Ion Battery. *Small* **2018**, *14*, 1703850. [CrossRef]
17. Islam, S.; Alfaruqi, M.H.; Song, J.; Kim, S.; Pham, D.T.; Jo, J.; Kim, S.; Mathew, V.; Baboo, J.P.; Xiu, Z.; et al. Carbon-coated manganese dioxide nanoparticles and their enhanced electrochemical properties for zinc-ion battery applications. *J. Energy Chem.* **2017**, *26*, 815–819. [CrossRef]
18. Xiong, T.; Zhang, Y.; Lee, W.S.V.; Xue, J. Defect Engineering in Manganese-Based Oxides for Aqueous Rechargeable Zinc-Ion Batteries: A Review. *Adv. Energy Mater.* **2020**, *10*, 2001769. [CrossRef]
19. Ma, K.; Li, Q.; Hong, C.; Yang, G.; Wang, C. Bi Doping-Enhanced Reversible-Phase Transition of α-MnO_2 Raising the Cycle Capability of Aqueous Zn–Mn Batteries. *ACS Appl. Mater. Interfaces* **2021**, *13*, 55208–55217. [CrossRef]
20. Dai, L.; Sun, Q.; Chen, L.; Guo, H.; Nie, X.; Cheng, J.; Guo, J.; Li, J.; Lou, J.; Ci, L. Ag doped urchin-like α-MnO_2 toward efficient and bifunctional electrocatalysts for Li-O_2 batteries. *Nano Res.* **2020**, *13*, 2356–2364. [CrossRef]
21. Lian, S.; Sun, C.; Xu, W.; Huo, W.; Luo, Y.; Zhao, K.; Yao, G.; Xu, W.; Zhang, Y.; Li, Z.; et al. Built-in oriented electric field facilitating durable Zn-MnO_2 battery. *Nano Energy* **2019**, *62*, 79–84. [CrossRef]

22. Han, M.; Qin, L.; Liu, Z.; Zhang, L.; Li, X.; Lu, B.; Huang, J.; Liang, S.; Zhou, J. Reaction mechanisms and optimization strategies of manganese-based materials for aqueous zinc batteries. *Mater. Today Energy* **2021**, *20*, 100626. [CrossRef]
23. Alfaruqi, M.H.; Islam, S.; Mathew, V.; Song, J.; Kim, S.; Tung, D.P.; Jo, J.; Kim, S.; Baboo, J.P.; Xiu, Z.; et al. Ambient redox synthesis of vanadium-doped manganese dioxide nanoparticles and their enhanced zinc storage properties. *Appl. Surf. Sci.* **2017**, *404*, 435–442. [CrossRef]
24. Zhao, Q.; Song, A.; Zhao, W.; Qin, R.; Ding, S.; Chen, X.; Song, Y.; Yang, L.; Lin, H.; Li, S.; et al. Boosting the Energy Density of Aqueous Batteries via Facile Grotthuss Proton Transport. *Angew. Chem. Int. Ed.* **2021**, *60*, 4169–4174. [CrossRef] [PubMed]
25. Kim, S.; Koo, B.-R.; Jo, Y.-R.; An, H.-R.; Lee, Y.-G.; Huang, C.; An, G.-H. Defect engineering via the F-doping of β-MnO_2 cathode to design hierarchical spheres of interlaced nanosheets for superior high-rate aqueous zinc ion batteries. *J. Mater. Chem. A* **2021**, *9*, 17211–17222. [CrossRef]
26. Zhang, Y.; Liu, Y.; Liu, Z.; Wu, X.; Wen, Y.; Chen, H.; Ni, X.; Liu, G.; Huang, J.; Peng, S. MnO_2 cathode materials with the improved stability via nitrogen doping for aqueous zinc-ion batteries. *J. Energy Chem.* **2022**, *64*, 23–32. [CrossRef]
27. Cai, X.; Bai, H.; Liu, Y.; Shi, W. Facile in situ synthesis of Ag and MnO_2 anchored on carbon microtubes for high-performance asymmetric supercapacitor applications. *Appl. Mater. Today* **2018**, *11*, 193–199. [CrossRef]
28. Panimalar, S.; Logambal, S.; Thambidurai, R.; Inmozhi, C.; Uthrakumar, R.; Muthukumaran, A.; Rasheed, R.A.; Gatasheh, M.K.; Raja, A.; Kennedy, J.; et al. Effect of Ag doped MnO_2 nanostructures suitable for wastewater treatment and other environmental pollutant applications. *Environ. Res.* **2022**, *205*, 112560. [CrossRef]
29. Wang, D.; Wu, J.; Liu, X.; Wu, L.; Ao, J.; Liu, W.; Sun, Y.; Zhang, Y. Formation of the front-gradient bandgap in the Ag doped CZTSe thin films and solar cells. *J. Energy Chem.* **2019**, *35*, 188–196. [CrossRef]
30. Li, Z.; Gu, A.; Lou, Z.; Sun, J.; Zhou, Q.; Chan, K.Y. Facile synthesis of iron-doped hollow urchin-like MnO_2 for supercapacitors. *J. Mater. Sci.* **2017**, *52*, 4852–4865. [CrossRef]
31. Cao, Q.; Gao, H.; Gao, Y.; Yang, J.; Li, C.; Pu, J.; Du, J.; Yang, J.; Cai, D.; Pan, Z.; et al. Regulating Dendrite-Free Zinc Deposition by 3D Zincopilic Nitrogen-Doped Vertical Graphene for High-Performance Flexible Zn-Ion Batteries. *Adv. Funct. Mater.* **2021**, *31*, 2103922. [CrossRef]
32. Li, J.; Shu, C.; Hu, A.; Ran, Z.; Li, M.; Zheng, R.; Long, J. Tuning oxygen non-stoichiometric surface via defect engineering to promote the catalysis activity of Co_3O_4 in Li-O_2 batteries. *Chem. Eng. J.* **2020**, *381*, 122678. [CrossRef]
33. Xu, J.-W.; Gao, Q.-L.; Xia, Y.-M.; Lin, X.-S.; Liu, W.-L.; Ren, M.-M.; Kong, F.-G.; Wang, S.-J.; Lin, C. High-performance reversible aqueous zinc-ion battery based on iron-doped alpha-manganese dioxide coated by polypyrrole. *J. Colloid Interface Sci.* **2021**, *598*, 419–429. [CrossRef]
34. Rahman, A.U.; Zarshad, N.; Wu, J.; Faiz, F.; Raziq, F.; Ali, A.; Li, G.; Ni, H. Fabrication of Ag-doped MnO_2 nanosheets@carbon cloth for energy storage device. *Mater. Sci. Eng. B* **2021**, *269*, 115150. [CrossRef]
35. Huang, J.; Wang, Z.; Hou, M.; Dong, X.; Liu, Y.; Wang, Y.; Xia, Y. Polyaniline-intercalated manganese dioxide nanolayers as a high-performance cathode material for an aqueous zinc-ion battery. *Nat. Commun.* **2018**, *9*, 2906. [CrossRef] [PubMed]
36. Oh, S.M.; Kim, I.Y.; Adpakpang, K.; Hwang, S.J. The beneficial effect of nanocrystalline and amorphous nature on the anode performance of manganese oxide for lithium ion batteries. *Electrochim. Acta* **2015**, *174*, 391–399. [CrossRef]
37. Gao, R.; Yang, Z.; Zheng, L.; Gu, L.; Liu, L.; Lee, Y.; Hu, Z.; Liu, X. Enhancing the Catalytic Activity of Co_3O_4 for Li–O_2 Batteries through the Synergy of Surface/Interface/Doping Engineering. *ACS Catal.* **2018**, *8*, 1955–1963. [CrossRef]
38. Cao, Y.; Lu, H.; Hong, Q.; Xu, B.; Wang, J.; Deng, Y.; Yang, W.; Cai, W. Synthesis of Ag/Co@CoO NPs anchored within N-doped hierarchical porous hollow carbon nanofibers as a superior free-standing cathode for Li-O_2 batteries. *Carbon* **2019**, *144*, 280–288. [CrossRef]
39. Qin, Y.; Wang, B.; Jiang, S.; Jiang, Q.; Huang, C.; Chen, H.C. Strongly anchored MnO nanoparticles on graphene as high-performance anode materials for lithium-ion batteries. *Ionics* **2020**, *26*, 3315–3323. [CrossRef]
40. Tan, Q.; Li, X.; Zhang, B.; Chen, X.; Tian, Y.; Wan, H.; Zhang, L.; Miao, L.; Wang, C.; Gan, Y.; et al. Valence Engineering via In Situ Carbon Reduction on Octahedron Sites Mn_3O_4 for Ultra-Long Cycle Life Aqueous Zn-Ion Battery. *Adv. Energy Mater.* **2020**, *10*, 2001050. [CrossRef]
41. Fang, G.; Zhu, C.; Chen, M.; Zhou, J.; Tang, B.; Cao, X.; Zheng, X.; Pan, A.; Liang, S. Suppressing Manganese Dissolution in Potassium Manganate with Rich Oxygen Defects Engaged High-Energy-Density and Durable Aqueous Zinc-Ion Battery. *Adv. Funct. Mater.* **2019**, *29*, 1808375. [CrossRef]
42. Ma, Y.; Ma, Y.; Diemant, T.; Cao, K.; Liu, X.; Kaiser, U.; Behm, R.J.; Varzi, A.; Passerini, S. Unveiling the Intricate Intercalation Mechanism in Manganese Sesquioxide as Positive Electrode in Aqueous Zn-Metal Battery. *Adv. Energy Mater.* **2021**, *11*, 2100962. [CrossRef]
43. Su, S.; Xu, Y.; Wang, Y.; Wang, X.; Shi, L.; Wu, D.; Zou, P.; Nairan, A.; Lin, Z.; Kang, F.; et al. Holey nickel nanotube reticular network scaffold for high-performance flexible rechargeable Zn/MnO_2 batteries. *Chem. Eng. J.* **2019**, *370*, 330–336. [CrossRef]
44. Zhou, J.; Dong, A.; Du, L.; Yang, C.; Ye, L.; Wang, X.; Zhao, L.; Jiang, Q. Mn-doped ZnO microspheres as cathode materials for aqueous zinc ion batteries with ultrastability up to 10 000 cycles at a large current density. *Chem. Eng. J.* **2021**, *421*, 127770. [CrossRef]

45. Le, S.; Zhang, L.; Song, X.; He, S.; Yuan, Z.; Liu, F.; Zhang, N.; Sun, K.; Feng, Y. Review—Status of Zinc-Silver Battery. *J. Electrochem. Soc.* **2019**, *166*, A2980–A2989. [CrossRef]
46. Jin, Y.; Zou, L.; Liu, L.; Engelhard, M.H.; Patel, R.L.; Nie, Z.; Han, K.S.; Shao, Y.; Wang, C.; Zhu, J.; et al. Joint Charge Storage for High-Rate Aqueous Zinc–Manganese Dioxide Batteries. *Adv. Mater.* **2019**, *31*, 1900567. [CrossRef]